

Optimizing Lunar Map Partitioning for Multipath Fade Loss Analyses

Ryan C. Toonen, *Member, IEEE*, Stephanie L. Booth, Bryan W. Welch, and Michael J. Zemba

Abstract—A methodology is presented pertaining to the run-time optimization of quasi-optical ray-tracing simulations. These shooting-and-bouncing ray methods are used for assessing multipath fade loss in cislunar communication links. Our approach employs partitioning lunar terrain maps in shapes that approximate two-dimensional projections of Fresnel zone cross-sections. This technique drastically reduces computational run-time without causing significant loss of simulation accuracy.

Keywords—Digital elevation models, Ray tracing, Interference, Multipath channels, Fading channels

I. INTRODUCTION

The goal of NASA’s Artemis Program is to send humans to the south pole region of the Moon by the mid-2020s.

The Artemis missions will rely, in part, on Direct-to-Earth (DTE) communication from the lunar surface to terrestrial ground-stations. Near the lunar south pole, the elevation angles involved in line-of-sight (LOS) antenna pointing to the Earth have relatively low values (typically not exceeding 7.5°), which results in significant lunar terrain scattering. The simultaneous arrival of LOS and scattered radio frequency (RF) signals (of non-negligible strength) at a receiver causes an effect known as multipath interference. This effect has been previously identified as a significant signal loss mechanism that should be taken into consideration when evaluating cislunar communication link budgets [1].

Multipath propagation effects are typically simulated using *shooting and bouncing ray* (SBR) methods in which electromagnetic (EM) waves are modeled as *rays*, complex-valued vectors containing amplitude, phase, and polarization information. In principle, multipath propagation could be simulated using EM models based on Maxwell’s equations. However, such simulations are often impractical to employ for scenarios involving vast terrains. Memory requirements can be prohibitively large; run-times can be impractically long; and when scattering surface models contain only *electrically-large* features (which are significantly larger than the EM wavelength λ under consideration), accuracy is often not significantly different than that resulting from a quasi-optical ray approximation (or SBR method) [2]. Although the

computational requirements of SBR methods are typically less stringent than those of numerical EM models (such as the finite element method), run-time can be excessively long if the simulation parameters are not carefully chosen.

For commonly used, commercial, ray-tracing engines (such as Ansys Savant and HFSS/SBR+)¹, run-time is directly proportional to the number of rays generated during an SBR simulation. When simulating multipath interference due to terrain scattering, ray-density is typically greater than or equal to the triangular mesh resolution of the three-dimensional (3D) terrain model [3], imported as a stereolithography (STL) file. Previously published work concerning cislunar multipath propagation has made use of lunar terrain models that spanned a radius of less than 10 km around a point of interest (POI) [1]. From our LOS simulations, we determined that geographical features at distances as far as 150 km from a POI cause visual obstruction, which leads to significant multipath fade loss for scenarios where the Earth appears on the moon’s horizon. *All other things being equal* and without consideration of secondary ray bounces, simulation run-time increases as the square of a relative increase in the span of a terrain model. So, expanding the range of the terrain model from a 10 km radius to a 150 km would increase simulation time by at least a factor of 225. In this work, we show that simulation run-time can be drastically reduced without loss of accuracy by partitioning the terrain maps in shapes that approximate two-dimensional (2D) projections of Fresnel zone cross-sections. We also present an overview of our methodology, which produces multipath fade loss parameters from 3D vehicle and terrain models and antenna EM models. These parameters can be used to generate frame error rate curves and estimate communication link budgets.

Prior efforts to reduce the run-time of ray-tracing simulations have focused on increasing algorithm efficiency rather than selectively partitioning digital elevation models (DEMs). Compared to the cislunar scenario, non-LOS indoor [4-6] and terrestrial outdoor [7] multipath-influenced cases are typically small in scale (less than 1 km in radius). Hence, there has not previously been a strong motivation to employ map partitioning. Our technique can be used in conjunction with

Ryan C. Toonen is with the NASA Glenn Research Center, Cleveland, OH 44135-3191 USA (e-mail: ryan.toonen@nasa.gov).

Stephanie L. Booth is with the NASA Glenn Research Center, Cleveland, OH 44135-3191 USA (e-mail: stephanie.l.booth@nasa.gov).

Bryan W. Welch is with the NASA Glenn Research Center, Cleveland, OH 44135-3191 USA (e-mail: bryan.w.welch@nasa.gov).

Michael J. Zemba is with the NASA Glenn Research Center, Cleveland, OH 44135-3191 USA (e-mail: michael.j.zemba@nasa.gov).

Color versions of one or more of the figures in this article are available online at <http://ieeexplore.ieee.org>

¹ Commercial software is identified in this paper only to adequately describe the considerations made in our analyses. Such identification implies neither recommendation or endorsement by the National Aeronautics and Space Administration, nor that the software identified is necessarily the best available for the described application.

other methods for reducing simulation run-time. For scenarios involving LOS communication links with low-elevation pointing of high-gain antenna beams over large distances (on the scale of 100 km) of rugged terrain, our method provides a means of quickly estimating which portions of a DEM will contribute significant scattering in a ray-tracing simulation.

II. METHODOLOGY

Fig. 1 is a flowchart of the steps used in our approach to cis lunar multipath fade loss analysis. The steps with red lettering are elaborated on in this work and include optimal partitioning of lunar terrain models, quasi-optical ray tracing (SBR simulation), and extraction of fade loss parameters.

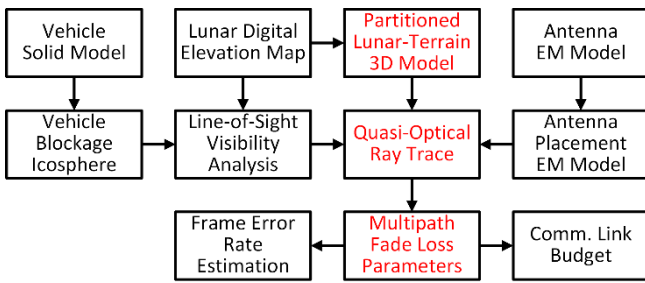


Fig. 1. Flowchart depicting the steps involved in cis lunar multipath fade loss analyses.

A. Initial Steps

Initial steps involve obtaining an EM model of the lunar transmitting antenna, a solid model of the lunar vehicle, and a lunar DEM pertaining to a POI (such as a potential landing site). The isolated antenna and vehicle models are used with computational SBR or EM simulators to generate an equivalent antenna model that accounts for scattering due to antenna placement on the vehicle. Results from an antenna placement analysis can be exported as a far-field radiation pattern or as a near-field model. Examples of near-field models include equivalent representation by a linear superposition of radiation from spherical point sources (such as a TICRA spherical wave expansion model [8]) or by an ensemble electric and magnetic short-dipole moments (such as an Ansys current-source model [9]). The vehicle model is also imported into a script [10] that determines visibility blockage caused by the vehicle from the point of view of the transmitting antenna. As output, the script generates a geodesic sphere whose faces indicate in a binary manner whether an observation direction is obstructed. The output file along with the lunar DEM is then imported into a software tool [11] that determines LOS visibility from the transmitting antenna to specified Earth-based ground-stations. The LOS simulation relies on a DEM extracted from raster image data obtained from NASA's Lunar Reconnaissance Orbiter / Lunar Orbiter Laser Altimeter missions [12]. The LOS visibility is determined by jointly assessing the ability for the Earth-based ground station and the lunar node to observe each other at all requested timesteps. This procedure requires that the lunar node is at an elevation angle greater than the elevation angle constraint of the Earth-based ground station from the

Earth-based ground station perspective, and it requires the Earth-based ground station to be above the lunar terrain-constrained horizon from the lunar node's perspective. Positions of the Earth and the Moon nodes, along with the required multiple body coordinate transformations, are calculated using the JPL NAIF SPICE Toolkit [13]. The curvature of the moon is accounted for when generating this 3D terrain model. The LOS simulation results include tables of observation (elevation and azimuth) angles for the specified time periods of a lunar mission.

B. Partitioning of Lunar Terrain Models

As depicted in Fig. 2, Fresnel zones are ellipsoidal surfaces that represent the locus of a point P such that the sum of the distances \overline{AP} (from a transmitter to point P) and \overline{PB} (from point P to a receiver) differs from the direct LOS path distance D by an amount equal to a half-integer multiple of the signal's wavelength, $n\lambda/2$. For cases where n is an even integer, the radial phase difference between rays that traversed the LOS and scattered paths is $0 \pmod{2\pi}$, and the resulting interference is constructive. Conversely, for cases where n is an odd integer, the phase difference is $\pi \pmod{2\pi}$, and the interference is destructive. Since Fresnel zones represent scattering boundaries whose points yield the same amount of interference (as detected by the receiver), we have rationalized that partitioning a lunar terrain model into the shape of a 2D projection of a Fresnel zone's cross-section should drastically reduce the amount of terrain that contributes insignificantly to the SBR simulations.

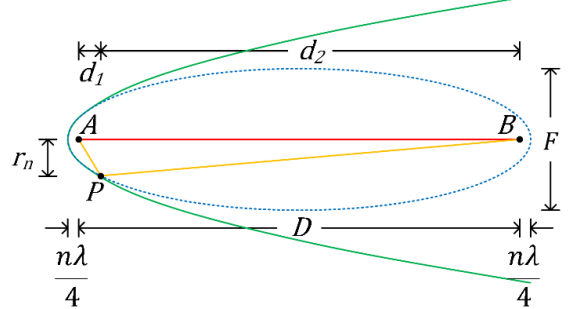


Fig. 2. Cross-section of n^{th} Fresnel zone (dotted ellipse) and its approximation (solid parabola) in the vicinity of the focus A .

The Fresnel zone cross-section is represented by an ellipse whose focal points indicate the locations of the transmitter and receiver – points A and B of Fig. 2, respectively. The minor-axis length is $F = \frac{1}{2}\sqrt{n\lambda D + \left(\frac{n\lambda}{2}\right)^2}$, and the major-axis length is $D + \frac{n\lambda}{2}$. For cases where $d_{1,max}$, the distance from the transmitter to the furthest lunar scattering point under consideration, is significantly less than the LOS distance D (roughly 358,460 km from the Moon to the Earth), we can approximate the Fresnel zones in the lunar vicinity using the

parabolic expression $r_n \approx \sqrt{n\lambda d_1 + \left(\frac{n\lambda}{2}\right)^2}$ where (d_1, r_n) represent the coordinates of the partitioned terrain boundary, and d_1 is measured in the direction of D .

> REPLACE THIS LINE WITH YOUR MANUSCRIPT ID NUMBER (DOUBLE-CLICK HERE TO EDIT) <

From simulations that employed DEM partitions with 2D projections of four different shapes, we analyzed ray-tracing results for self-consistency (by changing the observation angle for a given shape) and relative accuracy (by comparing the results of different shapes for a fixed observation angle). Fig. 3 illustrates (a) square, (b) circle, (c) sector, and (d) n^{th} Fresnel zone map partitions positioned at an arbitrary longitude (LON) and latitude (LAT). In comparison to the square partition, the circular projection provides a less anisotropic boundary, which is beneficial for simulations in which the azimuthal observation angle is varied over a wide range. However, both the square and circular partitions contain large amounts of area that do not significantly contribute to ray scattering from receiver's point of view. We explored the use of sector-shaped partitions with central angles equal to the half-power beamwidth (HPBW) of the transmitting antenna's radiation pattern. A buffer zone was required to include non-negligible ray-scattering from the near vicinity of the POI (the transmitter's location). However, a drawback of using the sector partition is that areas near the projection's edge contribute ray-scattering of decreasing significance as a function of distance away from the POI. The intention of employing the n^{th} Fresnel zone shape is to create a partition whose edge regions provide a more uniform distribution of ray-scattering significance.

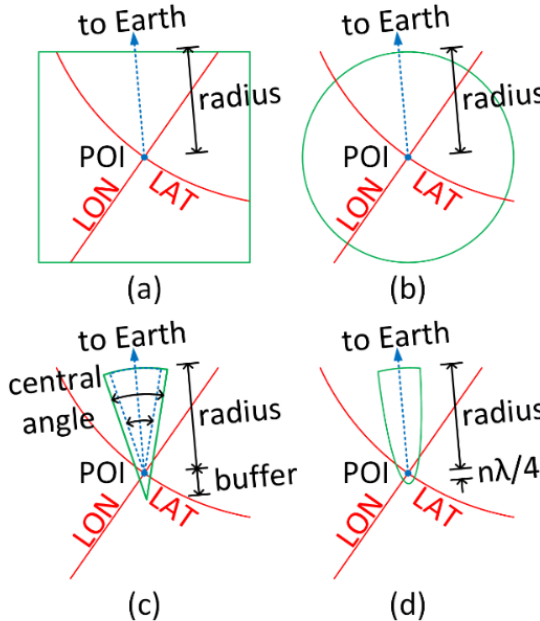


Fig. 3. (a) Square, (b) circle, (c) sector with a surrounding buffer zone, and (d) n^{th} Fresnel zone map partitions.

C. Quasi-Optical Ray-Tracing

Calculating the number of lattice points N in a partitioned DEM allows for a relative estimation of simulation run-time τ . Run-time is directly proportional to the number of ray bounces. The number of rays initially generated depends on the resolution μ (with units of meters per pixel) of the imported lunar DEM, the user-specified one-dimensional ray density η (with units of rays per wavelength), and the wavelength λ corresponding to the user-specified operating frequency. When the lunar DEM is

imported into the ray-tracing engine used in our studies, it is rendered as a surface of triangular facets. If the specified ray density does not exceed the one-dimensional facet edge density, then one ray is generated for every facet [3], as shown in Fig. 4 (a). Neglecting the influence of secondary ray bounces for this case, the run-time is directly proportional to the number DEM lattice points, $\tau \propto N$.

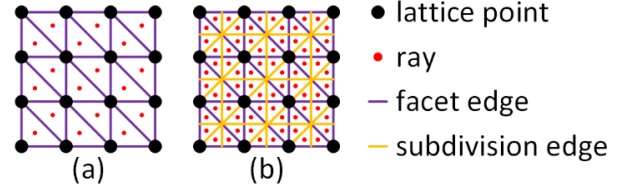


Fig. 4. Ray density for cases of (a) one ray per DEM facet and (b) one ray per DEM facet subdivision.

If the specified ray density does exceed the facet density, then the facet is subdivided into additional facets (without changing the curvature) so that facet density equals the ray density [3], as shown in Fig. 4 (b). Neglecting the influence of secondary bounces for this case, the run-time has the proportionality relationship of $\tau \propto N \cdot (\eta \cdot \mu/\lambda)^2$. So, for the same amount of terrain considered in a ray-tracing simulation, run-time would increase by at least the square of a relative increase in DEM resolution, ray density, or operating frequency.

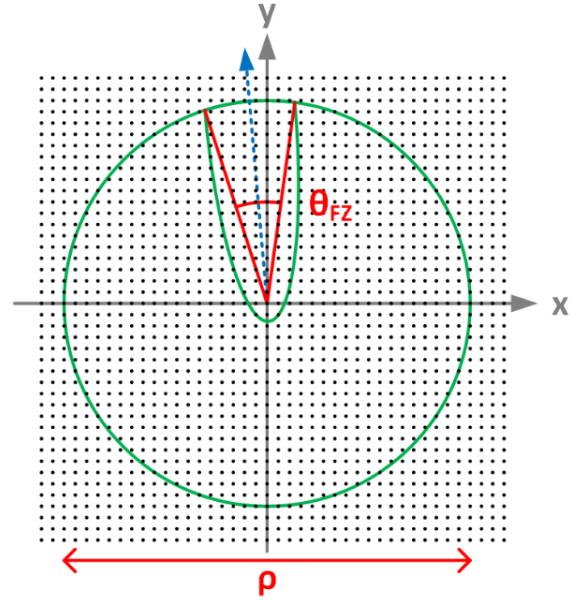


Fig. 5. Lattice points inscribed by a circle centered at the origin and a circle-cropped parabolic approximation of a Fresnel zone cross-section whose focus is positioned at the origin.

Fig. 5 shows a grid of lattice points inscribed by a circle centered at the origin of a Cartesian coordinate system. Also represented in this figure is a circle-cropped parabolic approximation of a Fresnel zone cross-section with an arbitrary orientation and a focus that is positioned at the origin. This model can be used to visualize the circle and Fresnel zone

> REPLACE THIS LINE WITH YOUR MANUSCRIPT ID NUMBER (DOUBLE-CLICK HERE TO EDIT) <

partitioning of a DEM. The number of DEM lattice points for a circular partition can be determined from the sum of a convergent series,²

$$N_c = 1 + 4 \sum_{i=0}^{\infty} \left(\left\lfloor \frac{\rho^2}{4i+1} \right\rfloor - \left\lfloor \frac{\rho^2}{4i+3} \right\rfloor \right), \quad (1)$$

where we have defined ρ as the partition radius scaled with respect to the DEM resolution, $\rho \equiv R_{DEM}/\mu$. We can estimate the number lattice points for the Fresnel zone partition by considering the ratio of shape areas,

$$N_{FZ} \approx \frac{A_{FZ}}{\pi \rho^2} N_c. \quad (2)$$

The area A_{FZ} of the circle-cropped parabolic approximation of the n^{th} Fresnel zone cross-section is given by

$$A_{FZ} = \frac{1}{6} \sqrt{n \xi} (4 \rho - n \xi)^{3/2} + \frac{\rho^2}{2} (\theta_{FZ} - \sin \theta_{FZ}), \quad (3)$$

where ξ represents operating wavelength scaled with respect to the DEM resolution, $\xi \equiv \lambda/\mu$. The angle θ_{FZ} is measured with respect to the origin between the points of intersection of the circle and the n^{th} Fresnel zone cross-section. It can be calculated with the equation

$$\theta_{FZ} = 2 \arctan \left[\sqrt{\left(1 - \frac{n \xi}{2 \rho} \right)^{-2} - 1} \right]. \quad (4)$$

D. Extracting Multipath Fade Loss Parameters

To gauge the influence of DEM partitioning on ray-tracing simulation results, we have employed the fading channel and terrain modeling assumptions of prior works [1,15]. These assumptions include characterizing the multipath fading channel with a wide-sense stationary uncorrelated scattering (WSSUS) model and treating the fading as being flat and slow. The assumption of *wide-sense stationarity* implies that a received signal can be treated as a complex random process with a mean power level and autocorrelation that do not vary with time. In the context of the problem under investigation, the *uncorrelated scattering* assumption implies that the terrain is composed of numerous points that scatter the transmitted signal with uncorrelated delay. An implication of the WSSUS assumption is that we should be able to fit (with reasonable confidence) short-term variations of the received signal power (or envelope) to a Rayleigh or Rician distribution.

The assumption of *flat* fading is appropriate if the channel's coherence bandwidth is significantly larger than the transmitted symbol rate. For such cases, it is justifiable to employ single-frequency ray-tracing. If the channel's coherence time is significantly larger than the symbol duration, then it is appropriate to model the fade as being *slow*. Under this assumption, it is justifiable to perform the ray-tracing with a static model. Terrain has been modeled as a uniform dielectric layer with a perfect electrical conductor backing [16,17].

To estimate fade loss parameters, multipath simulation data is generated from the point of view of the transmitting antenna.

As the Earth appears to move across the lunar sky, both the elevation $\epsilon[t]$ and azimuthal $\phi[t]$ observation angles are time dependent quantities. However, in the static approximation, we treat these variables with parametric representation. The total received complex envelope for a particular set of observation angles is the sum of rays from both the direct and scattered paths, $U_t[\epsilon, \phi] = U_d[\epsilon, \phi] + \sum_i U_{s,i}[\epsilon, \phi]$. In addition to having in-phase and quadrature parts, this data has the dimension of polarization. If the simulated data is generated in a basis of linear polarization, it can be represented in a basis of circular polarization using Jones vector analysis [18]. It follows that the right-handed and left-handed circularly polarized (RHCP and LHCP) complex amplitudes are respectively calculated from horizontal and vertical components by the expression

$$U_t^{(RHCP,LHCP)}[\epsilon, \phi] = \frac{U_t^{(H)}[\epsilon, \phi] \mp j U_t^{(V)}[\epsilon, \phi]}{\sqrt{2}}. \quad (5)$$

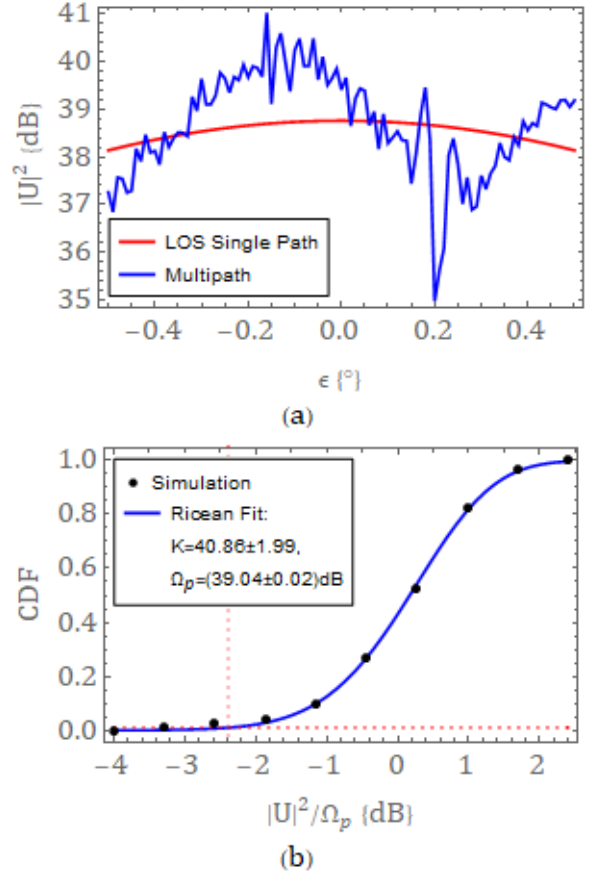


Fig. 6. (a) Relative LHCP power versus elevation angle. **(b)** CDF versus magnitude of scaled LHCP power. The dotted lines intersect at the coordinates of the $CL = 0.99$ fade loss.

With the azimuthal observation angle set to a fixed value, the direction in which the Fresnel zone DEM partition is oriented, U_t data is generated over a range of ϵ values. This process can

² The calculation stems from Gauss' Circle Problem: determine the number of lattice points inscribed by a circle centered at the origin and with a given radius (scaled with respect to the lattice spacing) [14].

> REPLACE THIS LINE WITH YOUR MANUSCRIPT ID NUMBER (DOUBLE-CLICK HERE TO EDIT) <

be repeated for different ϕ values. Pre-processed data $|u_t|$ is then obtained by removing the ϵ -dependent curvature of the envelope's magnitude by subtracting from it the magnitude of the direct path envelope. Removing the curvature allows for fade loss to be treated separately from pointing loss, and it enforces the WSSUS assumption of constant mean power. For processing convenience, the data set is then offset by the maximum magnitude of direct path rays and scaled with respect to the mean total envelope magnitude such that

$$|u_t[\epsilon]| = \frac{|U_t[\epsilon]| - |U_d[\epsilon]| + \max[|U_d[\epsilon]|]}{\text{mean}[|U_t[\epsilon]|]}. \quad (6)$$

For typical DTE downlinks, the LHCP component $u_t^{(LHCP)}$ is used in this calculation. A cumulative distribution function (CDF) histogram is then generated, and its points are fit to the Rician fading distribution,

$$F_{ric}[|u_t|] = 1 - Q_1\left[\frac{s}{\sqrt{b_0}}, \frac{|u_t|}{\sqrt{b_0}}\right]. \quad (7)$$

In this equation, Q_1 is the Marcum-Q function of first order, s^2 is the direct LOS ray power, and $2b_0$ is the power of all scattered rays. From the fitting parameters, we can obtain the Rice factor $K = s^2/2b_0$ and the average envelope power $\Omega_p = s^2 + 2b_0$ [1]. In the limit that K tends to zero, the Rician distribution becomes the Rayleigh distribution. Finally, a decibel estimate of fade loss, $20 \log_{10}[\alpha]$ dB, can be obtained by numerically solving for α in the expression $F_{ric}[\alpha] = 1 - CL$, where CL is the confidence level. So, if we wish to design a communication system for which the received signals will fall below the detection sensitivity level only 1% of the time, then we set $CL = 0.99$ and account for the resulting α value (in units of dB) as the fade margin of in our system.

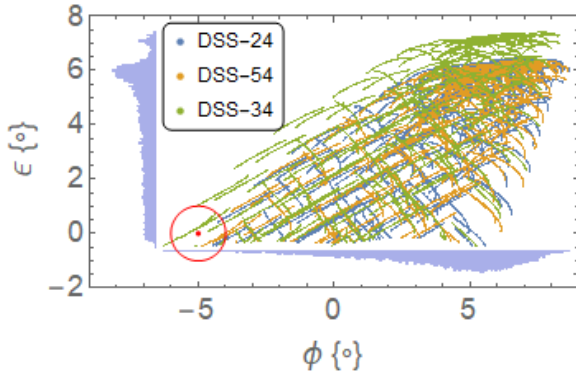


Fig. 7. Parametric plot of all LOS observation angle coordinates from the lunar south pole to the three DSN ground-stations for the year 2024. The red circle indicates the HPBW and a specific pointing direction of the transmitting antenna.

To illustrate the method of extracting multipath fade loss parameters from ray-tracing data, Fig. 6 (a) shows simulated direct-path and multipath envelopes plotted as a function of ϵ for a fixed ϕ . The simulations were executed with an operating frequency of 8.025 GHz, the low-end of the X-band frequency

allocation for DTE downlinks. The antenna model consisted of a parametric beam³ with a HPBW of $\theta_{HPBW} = 2.2025^\circ$, which corresponds to a 1 m diameter parabolic dish antenna at the stated operating frequency. The range of ϵ values should correspond to the observation angles over which the Earth-based ground-station will receive signals for a given antenna pointing direction. Modern tracking antennas typically have pointing accuracies of roughly $\pm 0.2^\circ$. So, we have limited the ϵ -range to 1° (several pointing accuracy values) with a resolution of 0.01° and the antenna pointed at the horizon ($\epsilon = 0^\circ$). The lunar terrain was modeled with a thickness of 10 m [16,19], and its material properties were described by a single relative dielectric constant and loss tangent [17], 3.7 and 0.01, respectively. These values were based on X-band laboratory characterizations of lunar regolith samples [16,20]. Fig. 6 (b) shows data points from a CDF histogram of the received, relative power points of Fig. 6 (a) scaled with respect to the mean Ω_p . A curve-fit revealed a Rice factor of $K = 40.86 \pm 1.99$ and a mean power of $\Omega_p = (39.04 \pm 0.02)$ dB. From these extracted parameters, the 99% confidence level, fade loss was determined to be $L_{99\%} = -2.386$ dB.

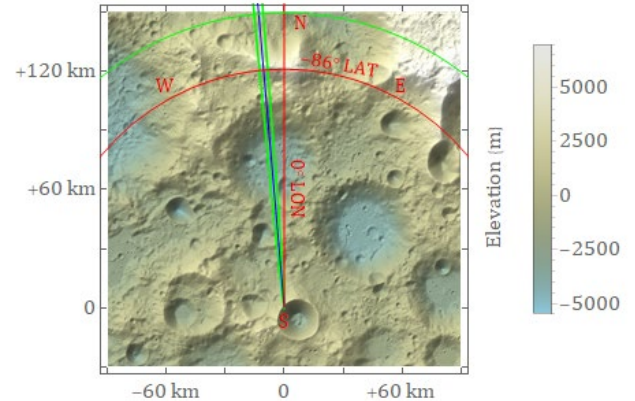


Fig. 8. A relief plot showing the terrain elevation near the POI.

III. CASE STUDY

To demonstrate the computational run-time savings achieved with DEM partitioning, we consider a fictional scenario in which a 1 m diameter, X-band transmitting antenna is placed 15 m above the surface of the exact lunar south pole. Fig. 7 displays the results of a visibility analysis that determined, for the year 2024, observation angles from the lunar POI to the three DSN ground-stations – Goldstone (DSS-24), Madrid (DSS-54), and Canberra (DSS-34). The terrain was modeled using a $\mu = 30$ meter-per-pixel DEM. Fig. 8, a relief plot of the terrain near the lunar south pole, shows that approximately 120 km from the POI is a mountain range (Malapert Massif) that causes LOS blockage to the DSN ground-stations. The intersection of the red lines indicates the approximate coordinates (-86° north latitude, 0° east longitude) of this obstruction. The blue solid blue line indicates an observation

³ The far-field, antenna gain pattern is given by $G[\phi] = \cos^m \phi$ where ϕ represents either ϵ or ϕ and $m \equiv \log_{10} 0.5 / \log_{10} [\cos[\theta_{HPBW}/2]]$ [21].

> REPLACE THIS LINE WITH YOUR MANUSCRIPT ID NUMBER (DOUBLE-CLICK HERE TO EDIT) <

azimuthal angle of $\phi = -5^\circ$ relative to the meridian. For reference, the green lines outline the $n = 1,000$ Fresnel zones and indicate a 150 km radius from the POI. Two sets of DEM partitions with radii of 5 km and 150 km were generated. Both sets included Fresnel zone projections with n values ranging between 10 and 1,000. Approximate optimization of Fresnel zone size was empirically determined by executing ray-tracing simulations for different n values and finding the point for which increasing this value negligibly changed the scattering data (as quantified by the $L_{99\%}$ fade loss). These results are presented in Fig. 9 and 10 for partition radii of 5 km and 150 km, respectively. The corresponding simulations made use of the same antenna and terrain modeling parameters that were used to generate the data of Fig. 6. Received far-field data was collected for ϵ ranging from -1.1° to $+1.1^\circ$ in 0.01° increments. The 221 data points were binned into a histogram of 11 points. A ray density of $\eta = 0.07$ rays/ λ was used and was similarly optimized by conducting a series of mini-experiments with a circular partition that involved varying η and finding the point of diminishing returns with respect to extracted fade loss.

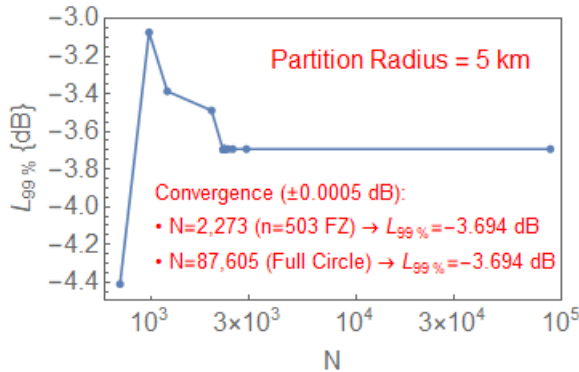


Fig. 9. 99% CI loss versus number of DEM pixels for the case of 5 km radius partitions.

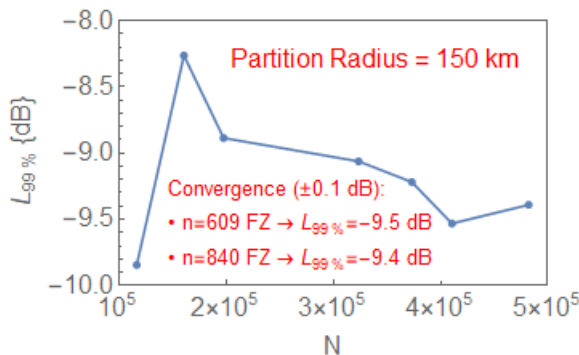


Fig. 10. 99% CI loss versus number of DEM pixels for the case of 150 km radius partitions.

For the case of 5-km radius partitions, the Fresnel zone results were compared those of a 5 km circular partition, which served as a baseline of accuracy. As indicated in Fig. 9, convergence of $L_{99\%}$ within ± 0.0005 dB was achieved for a Fresnel zone partition of $n = 503$. This partition contained

2,273 pixels, which is about thirty-nine times smaller than that of the full circular partition – having approximately 87,605 pixels. So, the computation times were different by at least a factor of thirty-nine. The 150 km radius case, as described by Fig. 10, displayed convergence at $n = 609$, within ± 0.05 dB for a 90% confidence interval (CI) and ± 0.1 dB for the 99% CI. This partition contained 410,541 pixels, which is approximately 191 times smaller than the 78,539,677 pixels of a full circular partition. The increased fade loss of the 150 km radius case shows that scattering from the distant mountain range is significant. Fig. 11 illustrates incident rays that scatter from the surface of the DEM to the far-field after one and two bounces (shown as green and blue lines, respectively). The high density of incident rays scattered from the mountain top visually emphasizes the importance of accounting for long-range, low-angle scattering in cislunar ray-tracing simulations.

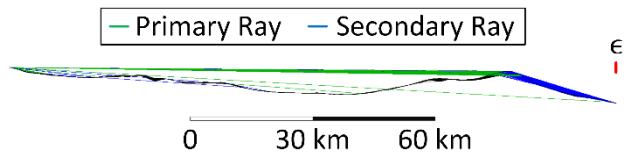


Fig. 11. Ray-tracing visualization for the 150 km radius DEM.

It is worth noting that the fade loss convergences corresponded to Fresnel zones whose extrapolated angles were comparable to the HPBW of the transmitting antenna. For the 5-km and 150-km radius cases, it we find that $\theta_{FZ} \approx 3 \theta_{HPBW}$ and $\theta_{FZ} \approx 0.6 \theta_{HPBW}$, respectively. As a *rule of thumb*, based on our experiences, we suggest initiating optimization studies with partitioned DEMs whose Fresnel zone indices produce extrapolated angles that fall within the approximate range of $\theta_{HPBW}/3 < \theta_{FZ} < 3 \theta_{HPBW}$. However, the near-optimized value of n depends on the desired convergence accuracy of a specific fade loss CI.

IV. CONCLUSION

We have empirically shown that partitioning lunar terrain models in the shape of Fresnel zone cross-sections drastically reduces simulation run-time without loss of accuracy. Near optimization of DEM partitioning can reduce simulation run time from weeks or days to just hours or minutes. We have incorporated this technique into our methodology for analyzing cislunar multipath propagation. To demonstrate the effectiveness of our methodology, we have presented a simplified, fictional scenario involving DTE from the exact lunar south pole to the Earth-based DSN ground-stations.

ACKNOWLEDGMENT

R. C. T. thanks Richard Reinhart (of NASA GRC) for his discussions on cislunar communications and Pete Serano (of Ansys, Inc.) for his insights on quasi-optical ray tracing.

NOTATION

A: coordinates of transmitter location

> REPLACE THIS LINE WITH YOUR MANUSCRIPT ID NUMBER (DOUBLE-CLICK HERE TO EDIT) <

A_{FZ} : area of a circle-cropped parabolic approximation of a Fresnel zone

B : coordinates of receiver location

b_0 : total half-power of all scattered rays

CDF: cumulative distribution function

CI: signal-detection confidence interval (or level) expressed as a percentage

CL: signal-detection confidence level

D : distance between a transmitter and a receiver

d_1 : distance along propagation axis from the transmitter location to an arbitrary scattering point along a Fresnel zone boundary

$d_{1,max}$: distance along propagation axis from the transmitter location to the furthest scattering point under consideration

d_2 : distance along propagation axis from an arbitrary scattering point along a Fresnel zone boundary to the receiver location

F : minor-axis length of an ellipse

F_{ric} : cumulative distribution function for Rician fading

G : far-field, antenna gain function

i : summation index

K : Rice factor

$L_{99\%}$: decibel fade loss for a 99% confidence interval

m : a substitution variable used when evaluating the far-field, antenna gain function

N : number of DEM lattice points

n : Fresnel zone index

N_C : number of lattice points for a DEM of a circular partition

N_{FZ} : number of lattice points for a DEM partitioned by a Fresnel zone parabolic approximation

P : coordinates of location of an arbitrary scattering point along a Fresnel zone boundary

Q_1 : first-order Marcum-Q function

R_{DEM} : radius of a circular DEM partition

r_n : distance from propagation axis to an arbitrary scattering point along a Fresnel zone boundary

s : square root of direct LOS ray power

t : time

U : complex amplitude of electric-field envelope of a ray

u : complex amplitude of electric-field envelope offset by a maximum value and scaled with respect to a mean value

x : a Cartesian ordinate

y : a Cartesian ordinate

α : linear fade loss value corresponding to a specific signal-detection confidence level

ϵ : elevation component of observation angle

η : one-dimensional ray density given in units of rays per wavelength

θ_{FZ} : angle between the points of intersection of a circle and the boundary of a Fresnel zone parabolic approximation taken with respect to the origin of a Cartesian coordinate system

θ_{HPBW} : divergence angle associated with an antenna's half-power beamwidth

λ : wavelength

μ : DEM length-per-pixel resolution

ξ : wavelength scaled with respect to DEM resolution

ρ : radius of a circular DEM partition scaled with respect to the DEM length-per-pixel resolution

τ : simulation run-time

φ : azimuthal or elevation component of observation angle

ϕ : azimuthal component of observation angle

Ω_p : mean ray power

REFERENCES

- [1] M. S. Net and K. -M. Cheung, "Mitigating Fading in Cislunar Communications: Application to the Human Landing System," *2020 IEEE Aerospace Conference*, 2020, pp. 1-11, doi: [10.1109/AERO47225.2020.9172778](https://doi.org/10.1109/AERO47225.2020.9172778).
- [2] Z. Yun and M. F. Iskander, "Ray Tracing for Radio Propagation Modeling: Principles and Applications," in *IEEE Access*, vol. 3, pp. 1089-1100, 2015, doi: [10.1109/ACCESS.2015.2453991](https://doi.org/10.1109/ACCESS.2015.2453991).
- [3] "Methodology Node" in *ANSYS Savant User Manual*, v. 2021 RI, p. 258 (2021).
- [4] Z. Ji, B.-H. Li, H.-X. Wang, H.-Y. Chen and T. K. Sarkar, "Efficient ray-tracing methods for propagation prediction for indoor wireless communications," in *IEEE Antennas and Propagation Magazine*, vol. 43, no. 2, pp. 41-49, April 2001, doi: [10.1109/74.924603](https://doi.org/10.1109/74.924603).
- [5] A. Bhuvaneshwari, R. Hemalatha, and T. Satya Savithri, "Development of an Optimized Ray Tracing Path Loss Model in the Indoor Environment," in *Wireless Pers Commun*, vol. 96, pp. 1039-1064, 2017, doi: [10.1007/s11277-017-4220-5](https://doi.org/10.1007/s11277-017-4220-5).
- [6] F. Hossain, T. K. Geok, T. A. Rahman, M. N. Hindia, K. Dimyati, S. Ahmed, C. P. Tso, and N. Z. Abd Rahman, "An Efficient 3-D Ray Tracing Method: Prediction of Indoor Radio Propagation at 28 GHz in 5G Network," in *Electronics*, vol. 8, no. 3, pp. 286-, 2019, doi: [10.3390/electronics8030286](https://doi.org/10.3390/electronics8030286).
- [7] S. Hu, L. -X. Guo and Z. -Y. Liu, "A Fast Ray-tracing Algorithm for Rugged Terrain," 2019 Cross Strait Quad-Regional Radio Science and Wireless Technology Conference (CSQRWC), 2019, pp. 1-3, doi: [10.1109/CSQRWC.2019.8799357](https://doi.org/10.1109/CSQRWC.2019.8799357).
- [8] C. Cappellin, O. Breinbjerg and A. Frandsen, "Properties of the transformation from the spherical wave expansion to the plane wave expansion," in *Radio Science*, vol. 43, no. 01, pp. 1-16, Feb. 2008, doi: [10.1029/2007RS003696](https://doi.org/10.1029/2007RS003696).
- [9] "Antenna Node" in *ANSYS Savant User Manual*, v. 2021 RI, p. 132-133 (2021).
- [10] M. Zemba, *Antenna Vision Master v. 1.5.0*. Cleveland: NASA Glenn Research Center, 2020.
- [11] B. Welch, *GRC Communication Analysis Software Suite (GCAS)*. Cleveland: NASA Glenn Research Center, 2020.
- [12] *Moon LRO LOLA DEM 118m v1 | USGS Astrogeology Science Center*, U. S. Geological Survey, Accessed on: Jun. 24, 2021. [Online]. Available:

> REPLACE THIS LINE WITH YOUR MANUSCRIPT ID NUMBER (DOUBLE-CLICK HERE TO EDIT) <

https://astrogeology.usgs.gov/search/details/Moon/LRO/LOLA/Lunar_LRO_LOLA_Global_LDEM_118m_Mar2014/cub.

- [13] SPICE: An Observation Geometry System for Space Science Missions, The Navigational and Ancillary Facility, Accessed on: Feb. 28, 2022. [Online]. Available: <https://naif.jpl.nasa.gov/naif/index.html>.
- [14] D. Hilbert and S. Cohn-Vossen, "Regular systems of points," in *Geometry and the Imagination*. New York, NY, USA: Chelsea Publishing Company, 1983, ch. 2, sec. 6, pp. 37–39.
- [15] M. S. Net, "Analysis of the Fading Channel in Downlinks from the Lunar South Pole to the Deep Space Network," in *The Interplanetary Network Progress Report*, vol. 42-216, pp. 1–30, Feb. 2019.
- [16] M. S. Net, "Multipath Fading on the Lunar South Pole," from *SCaN Technology Review*, Section 332 Communication Research & Architectures (February 10, 2019).
- [17] S. Hwu, M. Upanavage, and C. Sham, "Lunar surface propagation modeling and effects on communications." *26th International Communications Satellite Systems Conference (ICSSC)*, 2008, doi: [10.2514/6.2008-5495](https://doi.org/10.2514/6.2008-5495).
- [18] B. E. Saleh and M. C. Teich, *Fundamentals of Photonics*, 2nd ed. New York: Wiley, 203-204, 228 (2007).
- [19] B. M. French, G. Heiken, and D. Vaniman. *Lunar sourcebook: A user's guide to the Moon*. CUP Archive, pg. 93 (1991).
- [20] H. E. Bussey, "Dielectric measurements of lunar soil." in *Lunar and Planetary Science Conference*. vol. 9. (1978).
- [21] "Antenna Node" in *ANSYS Savant User Manual*, v. 2021 RI, p. 120 (2021).



Ryan C. Toonen (Member, IEEE) is a research and development engineer in the Systems Architecture and Analytical Studies Branch of the Communications and Intelligent Systems Division at the NASA Glenn Research Center. From the University of Wisconsin at Madison, he received the B.S. Applied Mathematics, Engineering and Physics (1999); B.S. Electrical Engineering (2002); M.S. Electrical Engineering (2005); M.A. Physics (2007); and Ph.D. Electrical Engineering (2007) degrees. He was previously a postdoctoral research associate at the National Institute of Standards and Technology (NIST), a research engineer at the U.S. Army Research Laboratory (ARL), and an assistant professor at the University of Akron (UA). While working at NIST, he contributed to an effort that led to the electronic re-definition of the Boltzmann constant. While working at ARL, he received the 2012 Army Research and Development Achievement (RDA) Award for Outstanding Technical Achievement. While he was with the UA, he led a nanoelectronic technologies research group. He left the UA upon receiving provost approval for tenure and promotion to the rank of associate professor. During his research career, he has gained expertise in the areas of applied physics, electronic devices and materials, and experimental microwave science. Prior to this career, he had worked in the field of mixed-signal application specific integrated circuits as a design engineer. He has been awarded three U.S. patents, and he is a recipient of the 2017 and 2018 NASA Glenn Research Center Faculty Fellowship Program award. He has authored and coauthored a number of refereed publications addressing a diverse range of topics that include: microwave device applications of graphene and carbon nanotube thin films, millimeter-wave investigations of magnetoelastic and multiferroic nano-materials, complex oxide physics, agile microwave engineering, applied superconductivity, quantum

dot transport, and instrumentation and measurement techniques.



Stephanie L. Booth is from Cleveland, Ohio. She obtained a bachelor's (2016) and master's (2017) of science from the University of Toledo in Toledo, Ohio for electrical engineering. Through her graduate studies, Stephanie focused on communication systems. She currently is a Systems Integrator at NASA Glenn Research Center within the Secure Networks, System Integration and Test Branch in the Communications and Intelligent Systems Division. Her work involves software defined networking, high temperature IC testing, free space optics, and link analyses.

Bryan W. Welch, photograph and biography not available at the time of publication.



Michael J. Zemba is a research engineer in the Advanced High Frequency Branch at NASA Glenn Research Center in Cleveland, Ohio. He has been at NASA since 2011. He received his Bachelor of Science in Electrical Engineering in 2011 and Master of Science in Electrical Engineering in 2013, both from the University of Akron. His research has included the study of atmospheric propagation at microwave frequencies, propagation for optical communications, and the additive manufacturing of antennas and electromagnetic structures. In addition, from 2017 to 2021 he served as the lead of independent verification & validation for the communications systems of the Power and Propulsion Element (PPE) of NASA's Gateway. Presently, he is the principal investigator for the MATRICS (Multiple Asset Testbed for Research in Innovative Communications Systems) emulation facility at Glenn Research Center, as well as a subject matter expert contributing to development of NASA's Lunar communications architecture under the Space Communication and Navigation (SCaN) office.